Harmonic Current and Inrush Fault Current Coordinated Suppression Method for VSG Under Non-ideal Grid Condition

Leming Zhou, *Member, IEEE*, Siyi Liu, *Student Member, IEEE*, Yandong Chen, *Senior Member, IEEE*, Weilang Yi, *Student Member, IEEE*, Shuke Wang, *Student Member, IEEE*, Xiaoping Zhou, *Member, IEEE*, Wenhua Wu, *Member, IEEE*, Jie Zhou, *Student Member, IEEE*, Chan Xiao, and Aoyang Liu

***Abstract*—For the virtual synchronous generator, the voltage-controlled harmonic suppression method will seriously deteriorate the magnitude of inrush fault current in the moment of grid symmetrical fault, because the suppression effects of harmonic current and inrush fault current are mutually constrained from the perspective of its output impedance. For this issue, a harmonic current and inrush fault current coordinated suppression method is proposed to achieve both good results of harmonic current suppression in normal grid and inrush fault current limitation in fault grid, which mainly includes a passive branch, an active branch and an improved virtual synchronous generator (VSG) control. The passive branch is installed between the PCC and grid to introduce an additional voltage variable. Meanwhile, with the proper feed-forward of the PCC voltage and additional voltage, the active branch is used to increase the mid/high frequency impedance viewed from the grid fault point to VSG, and also decrease the harmonic impedance viewed from the PCC to VSG. Then, not only the transient inrush fault current is limited, but also the harmonic current introduced from the nonlinear load is mostly absorbed. Moreover, the improved VSG control is used to limit the steady-state fundamental frequency fault current. Therefore, the contradictory between harmonic current and inrush fault current suppression for VSG is well solved. Finally, the experiment results validate the proposed control method.**

***Index Terms*—Harmonic current, nonideal grid, transient inrush fault current, virtual impedance, virtual synchronous generator (VSG).**

Manuscript received January 22, 2020; revised April 16, 2020; accepted June 2, 2020. Date of publication June 7, 2020; date of current version September 4, 2020. This work was supported in part by the Fundamental Research Funds for the National Natural Science Foundation of China under Grant 51707061, in part by the Central Universities under Grant 531118010260, in part by the Hunan Natural Science Foundation Funded Project under Grant 2018JJ3048, and in part by the Postdoctoral Innovative Talent Support Program of China under Grant BX20190109. Recommended for publication by Associate Editor P.-T. Cheng. *(Corresponding author: Siyi Liu.)*

Leming Zhou, Siyi Liu, Yandong Chen, Weilang Yi, Shuke Wang, Xiaoping Zhou, Wenhua Wu, Jie Zhou, and Chan Xiao are with the College of Electrical and Information Engineering, Hunan University, Changsha 410082, China (e-mail: leming_zhou@126.com; liusiyi641@hnu.edu.cn; yandong_chen@hnu.edu.cn; yiweilang@hnu.edu.cn; wangshuke@hnu.edu.cn; zxp2011@hnu.edu.cn; wenhua_5@163.com; zhoujiehnu@hnu.edu.cn; xiaochan00@hnu.edu.cn).

Aoyang Liu is with the Jingmen Electric Power Supply Corporation of the State Grid, Jingmen 448000, China (e-mail: 775179152@qq.com).

Color versions of one or more of the figures in this article are available online at https://ieeexplore.ieee.org.

Digital Object Identifier 10.1109/TPEL.2020.3000522

Nomenclature

VSG	Virtual synchronous generator.
DG	Distributed generation.
PGF	Point of grid fault.
HSM	Harmonic suppression method.
CSM	Coordinated suppression method.
LVRT	Low voltage ride through.

I. Introduction

VIRTUAL synchronous generator (VSG) technology can provide frequency and voltage support for the grid by simulating inertia and damping characteristics of synchronous machine, which improves the friendliness of distributed generation (DG) systems meaningfully [1]. Recently, the researches on VSG mainly focus on inertia, dynamic characteristics, stability, and other issues, but lack of the power quality issue [2]–[4]. Moreover, the power-electronic-based DGs are mainly located in remote areas, where the grid is nonideal. In this case, not only the grid current can be easily distorted by the increasing nonlinear loads/generations penetration, but also the voltage at the point of grid fault (PGF) will drop severely in the moment of grid short-circuit fault [5]–[7]. Then, the power quality of grid current and the stability of grid-connected system cannot be maintained, which will severely restrict the development and application of VSG.

For the harmonic current introduced by the nearby nonlinear load, the current-controlled harmonic suppression method (HSM) with the same amplitude and opposite phase is generally used to counteract it [8]–[11]. Especially in [11], the power quality of distribution networks can be well improved with the fast-dynamic response and less complexity current controller for properly injecting the harmonic current. However, the VSG has no internal current/voltage closed-loop control, so the current-controlled HSM with closed-loop control may be not suitable [12], [13]. For this, the virtual impedance concept is introduced to form a harmonic current circulation loop, e.g., a negative virtual impedance in series with the output impedance of DG unit [14], [15], or a virtual impedance paralleling with the output impedance of DG unit [16]. Moreover, literatures [17], [20] further proposes a voltage-controlled HSM with a negative

feed-forward of PCC voltage to largely scale down the output impedance of inverter, and then the nonlinear load current can be more absorbed by the VSG. But, no relevant analyses are presented about whether these abovementioned HSM methods affects the low voltage ride through (LVRT) capability during grid short-circuit fault. Especially for the VSG, the adverse influence of voltage-controlled HSM on the inrush fault current in the moment of grid symmetrical fault is required to be further researched.

Meanwhile, for the limitation of the inrush fault current under grid short-circuit fault condition, most researches mainly focus on the output-current-peak limitation schemes for the current-controlled or direct-power-controlled inverters by adjusting the active and reactive power control coefficients and maintaining the injected current within a safety value [21], [22]. But for the open-loop voltage-controlled VSG, these methods are difficult to implement since it has no inner current-loop. For this, literatures [23]–[25] proposes a mode switching method to suppress the inrush fault current by switching the VSG control to the closed-loop current control or *PQ* mode control in grid fault instant, but its detection delay for grid fault may lead to excessive transient inrush fault current and recovery current. To avoid the complicated control system, the inrush fault current can be suppressed by the fault current limiter topology and the dynamic voltage restorer, but these will increase the system losses and costs [26], [27]. Moreover, literatures [28]–[30] further proposes the transient inrush fault current suppression method based on the virtual impedance, because the inrush fault current can be limited by increasing the equivalent impedance viewed from the grid to VSG. Of course, the virtual impedance should be always introduced into the control system since the grid fault may occur randomly, otherwise the detection delay will result in an excessive instantaneous current. In this case, the power quality of grid current in normal grid may be affected by this virtual impedance, especially the control performance for VSG to absorb harmonic current introduced by nonlinear load, which needs to be further analyzed.

In this article, it is found that the inrush fault current will be seriously aggravated by the voltage-controlled HSM in the moment of grid symmetrical fault. Meanwhile, the requirements of VSG output impedance for the harmonic current suppression in normal grid and the inrush fault current limitation in fault grid are mutually constrained. To solve this issue, the article proposes a harmonic current and inrush fault current coordinated suppression method (CSM) for VSG. Therefore, the fault current restraint will not be affected by this HSM. Finally, the effectiveness of the proposed CSM is verified in the RTLAB platform.

II. Contradictory Between Harmonic Current and Inrush Fault Current Suppression for VSG Under Nonideal Grid

Fig. 1(a) shows the topology structure diagram of VSG under nonideal grid, where the VSG and the nonlinear load are located at PCC, and the grid short-circuit fault occurs between the PCC and grid side. Z_g, Z_{line}, Z_v represent the grid impedance, the

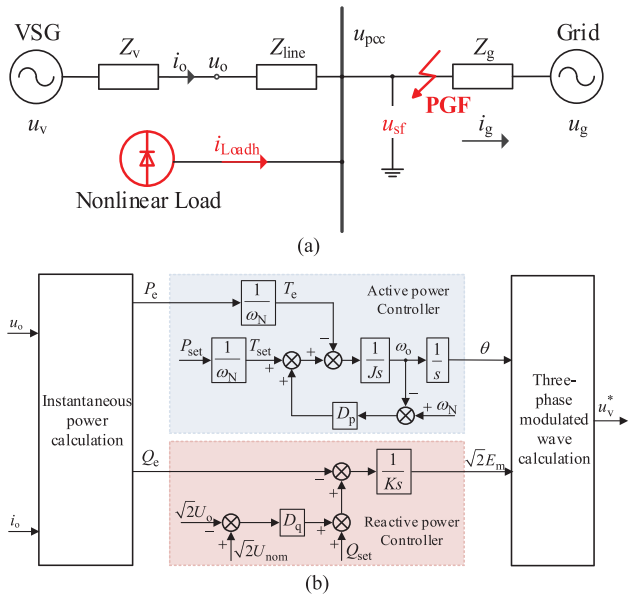

Fig. 1. System scheme diagram of VSG under nonideal grid. (a) System topology structure diagram. (b) Conventional control strategy diagram of voltage-controlled VSG.

line impedance and the VSG output impedance, respectively; u_g and i_g represent the grid voltage and grid current, respectively; u_{sf} represents the PGF voltage; u_o and i_o represent the output voltage and current of VSG, respectively; u_v represents the VSG terminal voltage; u_{pcc} represents the PCC voltage; and i_{Loadh} represents the nonlinear load current. Among them, u_v is approximately equal to the voltage reference of VSG (u^*_{v}).

Fig. 1(b) shows the control strategy of voltage-controlled VSG which emulates the inertia and damping characteristics of synchronous generator. The mathematical equations of the active power controller and reactive power controller of voltage-controlled VSG are as follows:

$$\begin{cases} P_{\text{set}}/\omega_N + (\omega_N - \omega_o)D_p - P_e/\omega_N = Js\omega_o = Js^2\theta \\ Q_{\text{set}} + \sqrt{2}D_q(U_{nom} - U_o) - Q_e = \sqrt{2}KsE_m \end{cases} \tag{1}$$

where P_{set} and Q_{set} represent the active and reactive power references, respectively; J represents the virtual moment of inertia; ω_o and ω_N represent the VSG output angular frequency and the grid rated angular frequency, respectively; D_p and D_q represent the coefficients of damping and voltage-drooping, respectively; P_e and Q_e represent the instantaneous active and reactive powers, respectively; θ represents the phase angle of the inner electric potential; K represents the inertia coefficient of reactive power loop; and U_{nom}, U_o and E_m represent the rms values of the rated voltage, the output voltage and the inner electric potential of VSG, respectively.

As shown in Fig. 1(a), when the grid is in normal operation, since the harmonic current introduced by the nonlinear load will deteriorate the power quality of i_g, it is expected that the harmonic current can be absorbed by VSG to improve the power quality of i_g. During grid short-circuit fault, it is expected that the inrush fault current can be effectively limited. Moreover, it

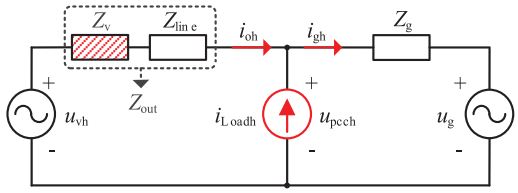

Fig. 2. Harmonic-domain circuit of VSG.

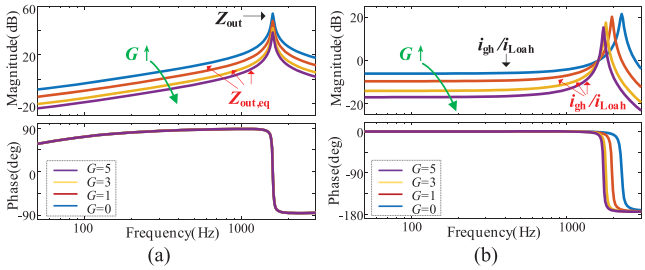

Fig. 3. Bode diagram of $Z_{\mathrm{out,eq}}$ and $i_{gh}/i_{\mathrm{Loadh}}$. (a) Bode diagram of $Z_{\mathrm{out,eq}}$. (b) Bode diagram of $i_{gh}/i_{\mathrm{Loadh}}$. (The solid blue line is $G = 0$, the solid red line is $G = 1$, the solid yellow line is $G = 3$, the solid purple line is $G = 5$.)

is also expected that the suppression methods for the harmonic current and the inrush fault current could be operated together instead of mode switching at different conditions, to avoid the excessive transient inrush current owing to fault detection delay.

A. Positive Effect of the Voltage-Controlled HSM for Harmonic Current Suppression

Fig. 2 shows the harmonic-domain circuit of VSG connected to nonideal grid, where each voltage or current variable with the subscript h is defined as its harmonic component. In harmonic-domain, the nonlinear load is equivalent to a harmonic current source, while the VSG is equivalent to a harmonic voltage source. According to Thevenin theorems, the expression of i_{gh} is obtained by harmonic sources superposition as

$$i_{gh} = \frac{Z_{\mathrm{out}}}{Z_g + Z_{\mathrm{out}}} \cdot i_{\mathrm{Loadh}} + \frac{1}{Z_g + Z_{\mathrm{out}}} \cdot u_{vh}. \tag{2}$$

Based on (2), it can be noted that $i_{gh}/i_{\mathrm{Loadh}}$ is proportional to Z_{out}. That is: the smaller Z_{out} is, the smaller $i_{gh}/i_{\mathrm{Loadh}}$ is, and the less influence of nonlinear load current on the power quality of grid current.

According to the positive correlation between harmonic current and output impedance, the voltage-controlled HSM with the negative feed-forward of PCC voltage is presented for VSG to largely scale down the Z_{out}, such as [17]–[20]. By this way, the nonlinear load harmonic current can be mostly absorbed. The reshaped VSG output impedance is expressed as

$$Z_{\mathrm{out,eq}} = \frac{Z_{\mathrm{out}}}{1 + G} \tag{3}$$

where G represents the negative feed-forward coefficient of PCC voltage, $G > 0$.

The bode diagram of $Z_{\mathrm{out,eq}}$ is shown as Fig. 3(a), and the bode diagram of $i_{gh}/i_{\mathrm{Loadh}}$ is shown as Fig. 3(b), where the different curve color represents different value of G. It can be seen that the larger G is, the smaller $Z_{\mathrm{out,eq}}$ is, and the smaller $i_{gh}/i_{\mathrm{Loadh}}$ is. Therefore, it is expected that the VSG output impedance is small to obtain better power quality of grid current.

B. Negative Effect of the Voltage-Controlled HSM for the Inrush Fault Current Limitation

Fig. 4(a) shows the equivalent impedance circuit of VSG in fault grid with the voltage-controlled HSM in [17]–[20], where $Z_{\mathrm{out,eq}}$ represents the reshaped impedance viewed from the PGF to VSG with this HSM; Z_{out} represents the original impedance viewed from the PGF to VSG without this HSM; u_s

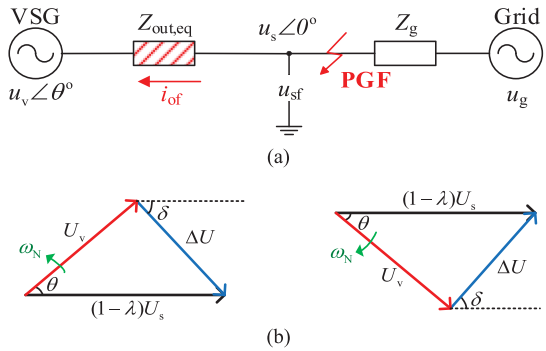

Fig. 4. Circuit diagram and voltage phasor diagram of VSG in fault grid. (a) Equivalent impedance circuit. (b) Voltage phasor diagram.

and u_{sf} represent the PGF voltages before and after the fault, respectively; u_v represents the VSG terminal voltage; and each voltage or current variable with the subscript f is defined as its fault component. Among them, R' and L' represent the resistance and inductance of $Z_{\mathrm{out,eq}}$, respectively; $\varphi' = \arctan(\omega L'/R')$ represents the angle of $Z_{\mathrm{out,eq}}$; R and L represent the resistance and inductance of Z_{out}, respectively; $\varphi = \arctan(\omega L/R)$ represents the angle of Z_{out}. There is $Z_{\mathrm{out,eq}} = Z_{\mathrm{out}}/(1 + G)$, so $\varphi' = \varphi$. Here, the adverse effect of reshaped VSG output impedance on inrush fault current in the moment of grid symmetrical fault is analyzed in detail.

When fault occurs, the fault current i_{of} can be expressed as

$$R' \cdot i_{of} + L' \cdot \frac{di_{of}}{dt} = \Delta u \tag{4}$$

where Δu represents the voltage drop from the PGF to VSG.

Taking Phase A as example, the PGF voltage after the fault is expressed as follows:

$$u_{sf} = \sqrt{2}U_{sf}\ \sin(\omega_N t) = \sqrt{2}(1-\lambda)U_s\ \sin(\omega_N t) \tag{5}$$

where U_{sf} and U_s represent the rms values of u_{sf} and u_s, respectively; and λ represents the voltage drop depth at the PGF.

According to Appendix, the voltage drop from the PGF to VSG mainly depends on the voltage drop at the PGF, there is

$$\begin{aligned}\Delta u &= \sqrt{2}(1-\lambda)U_s\ \sin(\omega_N t) - \sqrt{2}U_v\ \sin(\omega_N t + \theta) \\ &= \sqrt{2}\Delta U\ \sin(\omega_N t + \delta)\end{aligned} \tag{6}$$

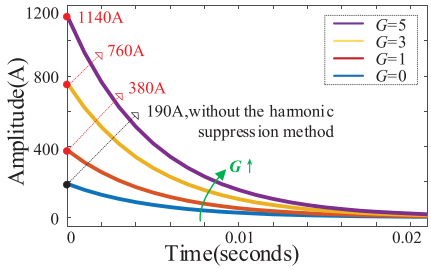

Fig. 5. Curve of transient inrush fault current i_{ot} with the voltage-controlled HSM in [17]–[20], $\lambda = 0.2$, $R = 0.2\ \Omega$, $L = 1$ mH. (The solid blue line is $G = 0$, the solid red line is $G = 1$, the solid yellow line is $G = 3$, the solid purple line is $G = 5$.)

where, U_v, ΔU represent the rms values of u_v and Δu, respectively; and δ represents the phase angle of Δu.

According to the voltage phasor diagram shown in Fig. 4(b), ΔU and δ can be obtained by cosine and sine theorems as

$$\begin{cases} \Delta U = \sqrt{[(1-\lambda)U_s]^2 + (U_v)^2 - 2(1-\lambda)U_s U_v \cos\theta} \\ \delta = -\arcsin\frac{U_v \sin\theta}{\Delta U}. \end{cases} \tag{7}$$

Based on (4)–(7), the fault current $i_{\rm of}$ is obtained as

$$\begin{aligned} i_{of} &= I_{pm}\sin(\omega_N t + \delta - \varphi) + (I_m - I_{pm})\sin(\delta - \varphi)e^{-t/\tau} \\ &= i_{os} + i_{ot} \end{aligned} \tag{8}$$

where $\tau = L'/R' = L/R$ represents the time constant of transient component attenuation; i_{os} and i_{ot} represent the steady-state and transient components of $i_{\rm of}$, respectively; and I_{pm} and I_m represent the amplitudes of i_{os} and i_o, respectively. Among them, I_{pm} and I_m are expressed as

$$\begin{cases} I_{pm} = \dfrac{\sqrt{2}\Delta U}{\sqrt{R'^2 + (\omega L')^2}} = \dfrac{\sqrt{2}(1+G)\Delta U}{\sqrt{R^2 + (\omega L)^2}} \\ I_m = \dfrac{\sqrt{2}\Delta U_{(\lambda=0)}}{\sqrt{R'^2 + (\omega L')^2}} = \dfrac{\sqrt{2}(1+G)\Delta U_{(\lambda=0)}}{\sqrt{R^2 + (\omega L)^2}}. \end{cases} \tag{9}$$

Based on (8) and (9), the transient inrush fault current i_{ot} can be expressed as

$$i_{ot} = \left[\frac{\sqrt{2}(1+G)(\Delta U_{(\lambda=0)} - \Delta U)}{\sqrt{R^2 + (\omega L)^2}}\right]\sin(\delta - \varphi)e^{-t/\tau}. \tag{10}$$

Meanwhile, the steady-state fault current i_{os} is expressed as

$$i_{os} = \frac{\sqrt{2}(1+G)\Delta U}{\sqrt{R^2 + (\omega L)^2}}\sin(\omega_N t + \delta - \varphi). \tag{11}$$

Based on (10), the curve of transient inrush fault current i_{ot} is shown as Fig. 5, where the different curve color represents different value of G. Obviously, the reshaped VSG output impedance results in higher amplitude of i_{ot} and i_{os}, and the larger G is, the larger i_{ot} and i_{os} are. It means that the voltage-controlled HSM will aggravate the transient inrush fault current and steady-state fault current in the moment of grid symmetrical fault, which apparently has an adverse effect on the system's LVRT capability.

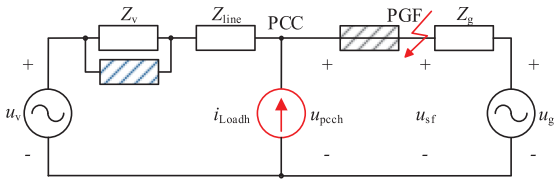

Fig. 6. Desiring impedance-based coordinated suppression scheme of the harmonic current and the transient inrush fault current.

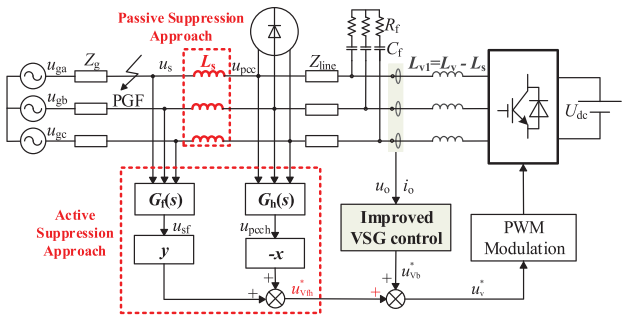

Fig. 7. Comprehensive control diagram of the proposed CSM.

Moreover, in summary of Section II-A and Section II-B, it can be concluded that reducing $Z_{\rm out}$ can suppress i_{gh}, but $i_{\rm of}$ will turn larger; increasing $Z_{\rm out}$ can limit $i_{\rm of}$, but i_{gh} will be more distorted. Therefore, it is contradictory to suppress $i_{\rm of}$ and i_{gh} from the perspective of changing $Z_{\rm out}$. i_{of} and i_{gh} cannot be reduced effectively just by adjusting $Z_{\rm out}$.

That is, the requirements for VSG output impedance are mutually constrained when considering both harmonic current suppression in normal grid and inrush fault current limitation in fault grid. Hence, it is necessary to find a suitable CSM to improve the adaptability of VSG connected to non-ideal grid.

III. CSM for Harmonic Current and Inrush Fault Current

To improve the adaptability of VSG under nonideal grid condition, an impedance-based CSM for harmonic current and inrush fault current is proposed. The design approach is shown in Fig. 6, where the output impedance viewed from the PCC to VSG can be reduced by Z_v paralleling with a virtual impedance to suppress the grid harmonic current; the equivalent impedance viewed from the PGF to VSG can be increased by string a large virtual impedance to limit the inrush fault current. The comprehensive control diagram is shown as Fig. 7, which mainly includes a passive branch, an active branch and an improved VSG control. The control diagram of the improved VSG control is shown in Fig. 8.

As shown in Fig. 7, the passive branch separated from the decentralized filter inductor is installed between the PCC and the grid for introducing an additional voltage variable u_s, which is similar to *LCL* filter. Of course, the limitation of passive branch should be also emphasized: a larger voltage drop on the passive branch will be formed with the increase numbers of parallel inverters. But for only one VSG, it will not add any voltage drop on the passive branch.

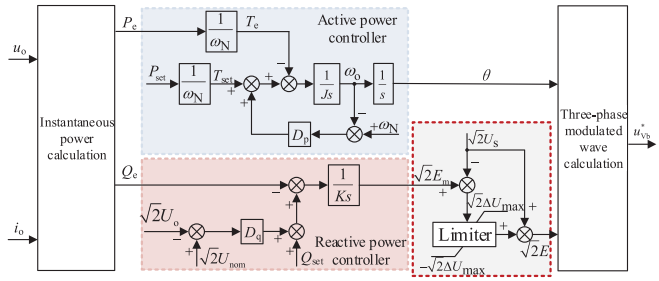

Fig. 8. Control diagram of the improved VSG control.

Then, through the proper feed-forwards of $u_{\rm pcc}$ and u_s, the active branch can reduce the harmonic impedance viewed from the PCC to VSG, and increase the mid/high frequency impedance viewed from the PGF to VSG. Moreover, the improved VSG control can increase the fundamental frequency impedance viewed from the PGF to VSG. Therefore, the contradictory between harmonic current and inrush fault current suppression for VSG is well solved.

Here, $u_{\rm pcch}$ represents the harmonic component of $u_{\rm pcc}$, considering that the harmonic current introduced by the nonlinear load may contain many harmonic frequencies including the major harmonics and inter-harmonics, it is obtained by the difference between $u_{\rm pcc}$ and its fundamental component [31]; u_{sf} represents the fault component of u_s, which is obtained through the high-pass filter. The feed-forward coefficient (-x) of $u_{\rm pcch}$ is negative, and the feed-forward coefficient (y) of u_{sf} is positive.

Based on Fig. 7, the coordinated harmonic and fault voltage reference of VSG ($u^*_{\rm Vfh}$) is controlled by using u_{pcch} and u_{sf}, expressed as

$$u^*_{Vfh}(s) = -xG_h(s)\cdot u_{\rm pcch}(s) + yG_f(s)\cdot u_{sf}(s) \tag{12}$$

where $G_h(s)$ and $G_f(s)$ are the equivalent transfer functions of the harmonic and fault components extraction, respectively, expressed as

$$\begin{cases} G_h(s) = 1 - \frac{\omega_{c1}(s+\omega_{c1})}{s^2+2\omega_{c1}s+(\omega_{c1}^2+\omega_N^2)} \\ G_f(s) = \frac{k\cdot s^2}{s^2+2\xi\omega_{c2}s+\omega_{c2}^2} \end{cases} \tag{13}$$

where ξ is the damping coefficient of the second-order high-pass filter, and its value is 0.7; k is the gain; and ω_{c1} and ω_{c2} are the cut-off frequencies of the harmonic extraction function and the fault extraction function, respectively. Based on (13), it is derived that $|G_h(j\omega_{c1})| = |G_f(j\omega_{c2})| = 1$.

As shown in Fig. 8, E represents the inner electric potential rms of the improved VSG. The voltage difference between E_m and U_s is limited by the Limiter: $|E_m - U_s| \le \Delta U_{\max}$. Then, E satisfies: $E = |E_m - U_s| + U_s$. By this way, the difference between the fundamental components of u_v and u_s can be restricted. So, the steady-state fundamental frequency fault current can be limited. Here, $\Delta U_{\max}$ is restricted as

$$\Delta U_{\max} \le 1.5I_{\rm oN}\cdot(j\omega L_s + Z_{\rm out}) \approx 1.5I_{\rm oN}\cdot\omega L_v \tag{14}$$

where $I_{\rm oN}$ represents the rms value of the rated output current of VSG.

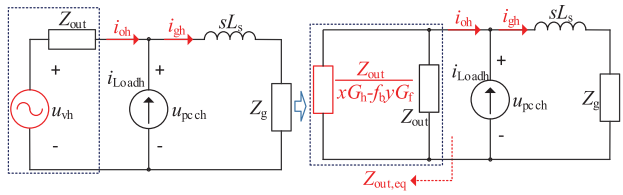

Fig. 9. Equivalent harmonic-domain circuits only considering the nonlinear load.

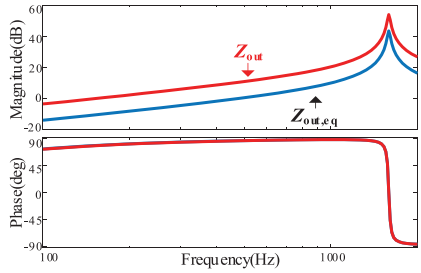

Fig. 10. Bode diagram of the equivalent output impedance $Z_{\rm out,eq}$, $x = 2.4$, $y = 0.1$.

To facilitate the analysis of the proposed CSM, it will be divided into two cases of only the nonlinear load in normal grid and only the grid short-circuit fault.

A. Principle and Effectiveness of the Proposed CSM in Condition of the Nonlinear Load

Assuming the grid is in normal operation, it only considers the effect of the nonlinear load harmonic current $i_{\rm Loadh}$. The principle and effectiveness of the proposed CSM to suppress the grid harmonic current is analyzed from the perspective of impedance as follows.

Based on (12), i_{oh} can be expressed as

$$i_{oh} \approx \frac{u^*_{Vfh} - u_{\rm pcch}}{Z_{\rm out}} = \frac{-(1+xG_h)\cdot u_{\rm pcch} + yG_f\cdot u_{sf}}{Z_{\rm out}} \tag{15}$$

where

$$u_{sf} = \frac{Z_g}{Z_g + sL_s}\cdot u_{\rm pcch} = f_b\cdot u_{\rm pcch}. \tag{16}$$

Based on (15) and (16), the equivalent output impedance viewed from the PCC to VSG can be obtained as

$$\begin{aligned} Z_{\rm out,eq} &= -\frac{u_{\rm pcch}}{i_{oh}} = \frac{Z_{\rm out}}{1+(xG_h - f_b yG_f)} \\ &= Z_{\rm out}//\frac{Z_{\rm out}}{xG_h - f_b yG_f}. \end{aligned} \tag{17}$$

Based on (17), the equivalent harmonic-domain circuits only considering the nonlinear load is depicted in Fig. 9, and the bode diagram of $Z_{\rm out,eq}$ is shown in Fig. 10. Apparently, on the basis of (17), Figs. 9 and 10, it is noted that the equivalent output impedance $Z_{\rm out,eq}$ at harmonic frequencies is proportional to the parallel virtual impedance $Z_{\rm out}/(xG_h - f_b yG_f)$. Then, the harmonic impedance viewed from the PCC to VSG can be

reduced by controlling the coefficients $(-x, y)$ properly. Thereby, i_{gh} is suppressed since the harmonic current introduced by nonlinear load is largely absorbed by VSG, expressed as

$$i_{gh} = \frac{Z_{\text{out,eq}} \cdot i_{\text{Loadh}}}{sL_s + Z_g + Z_{\text{out,eq}}} = \frac{Z_{\text{out}} \cdot i_{\text{Loadh}}}{(1 + xG_h - f_b y G_f) \cdot (sL_s + Z_g) + Z_{\text{out}}}. \quad (18)$$

B. Principle and Effectiveness of the Proposed CSM in Condition of the Grid Fault

During grid symmetrical short-circuit fault, considering the influence of grid voltage drop depth, the principle and effectiveness of the proposed CSM to limit the transient and steady-state fault current is analyzed from the perspective of impedance as follows.

Based on (13), the active branch only changes the mid/high frequency impedance characteristics because the fundamental components introduced by $G_f(s)$ and $G_h(s)$ tend to be very small, thus its influence on fundamental frequency impedance during the fault steady-state process can be neglected. On the contrary, the improved VSG control part of the proposed CSM only changes the fundamental frequency impedance characteristics since it is established from the steady-state circuit ignoring the effect of transient component, thereby its influence during the fault transient process can be neglected.

Therefore, the mid/high frequency impedance during fault transient process and the fundamental frequency impedance during fault steady-state process can be analyzed as follows.

1) Analysis of Mid/High Frequency Impedance Characteristics:: Based on (12), the inrush fault current i_{of} is expressed as

$$i_{of} = \frac{u_v - u_{sf}}{Z_{\text{sum}}} \approx \frac{u^*_{Vfh} - u_{sf}}{Z_{\text{sum}}} = \frac{-xG_h \cdot u_{pcch} + (yG_f - 1) \cdot u_{sf}}{Z_{\text{sum}}} \quad (19)$$

where Z_{sum} is equal to the sum of L_s and Z_{out}.

Moreover, according to the KCL principle, there is

$$\frac{u_{sf} - u_{\text{pcch}}}{sL_s} = \frac{u_{\text{pcch}} - u_v}{Z_{\text{out}}} \Rightarrow u_{pcch} \approx \frac{Z_{\text{out}} + yG_f sL_s}{Z_{\text{out}} + (1 + xG_h)sL_s} u_{sf}. \quad (20)$$

Based on (19) and (20), the mid/high frequency impedance viewed from the PGF to VSG can be derived as

$$Z_{\text{sum},eqh} = -u_{sf}/i_{of} = f_h \cdot Z_{\text{sum}} \quad (21)$$

where

$$f_h = \frac{1}{1 + \frac{xG_h \cdot (Z_{\text{out}} + yG_f sL_s)}{Z_{\text{out}} + (1 + xG_h) \cdot sL_s} - yG_f}. \quad (22)$$

Based on (21), the equivalent mid/high frequency impedance circuits under the grid short-circuit fault condition is depicted in Fig. 11. It is noted that $Z_{\text{sum},eqh}$ can be enlarged by the parameter

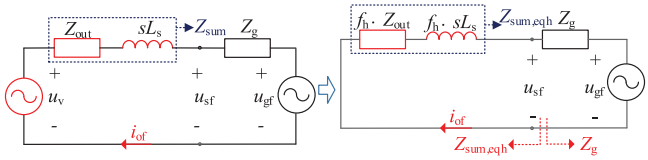

Fig. 11. Equivalent mid/high frequency impedance circuits under the grid fault.

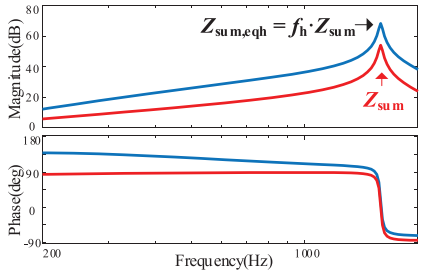

Fig. 12. Bode diagram of the mid/high frequency impedance $Z_{\text{sum},eqh}$, $x = 0.2$, $y = 1$.

f_h. And, when $y = 1 + x$, the denominator of f_h will be close to 0, which means that $Z_{\text{sum},eqh}$ is theoretically infinite.

The bode diagram of the mid/high frequency impedance $Z_{\text{sum},eqh}$ viewed from the PGF to VSG is depicted in Fig. 12. It can be found that the amplitude of $Z_{\text{sum},eqh}$ at mid/high frequency band is significantly increased, thus the transient inrush fault current can be effectively restricted.

2) Analysis of Fundamental Frequency Impedance Characteristic: In Fig. 8, if the output of the limiter is $|\Delta U_{\max}|$, there is

$$\Delta U_{\max} = |U_{sf} - U_v|. \quad (23)$$

Thus, the steady-state fault current I_{os} can be obtained as

$$I_{os} = \frac{\Delta U_{\max}}{k \cdot Z_{\text{sum}}} = \frac{|U_{sf} - U_v|}{k \cdot Z_{\text{sum}}} \quad (24)$$

where k represents the fundamental frequency impedance amplification factor.

Based on (24), the fundamental frequency impedance viewed from the PGF to VSG can be derived as

$$Z_{\text{sum},eqf} = k \cdot Z_{\text{sum}}. \quad (25)$$

In engineering practice, the current safety limit value can be set as $I_{os} \le 1.5 I_{\text{oN}}$, so

$$\frac{|U_{sf} - U_v|}{k \cdot Z_{\text{sum}}} = 1.5 * I_{\text{oN}} = 1.5 * \frac{|U_s - U_v|}{Z_{\text{sum}}}. \quad (26)$$

Based on (26), the factor k can be derived as

$$k = \frac{|U_{sf} - U_v|}{1.5 * |U_s - U_v|}. \quad (27)$$

According to (27), it is obvious that the larger k is, the larger $Z_{\text{sum},eqf}$ is, so the effect of limiting the steady-state fundamental frequency fault current is better.

Based on (23), the critical value of λ can be solved as: $\lambda_o = 0.0517$. If $\lambda < \lambda_o$, the output of the limiter is less than $|\Delta U_{\max}|$,

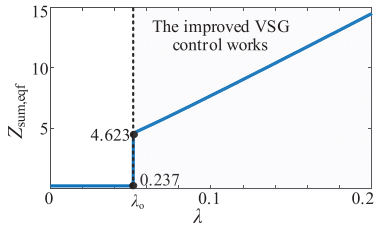

Fig. 13. Curve of the fundamental frequency impedance $Z_{\mathrm{sum},eqf}$, $x = 5$, $y = 5.1$.

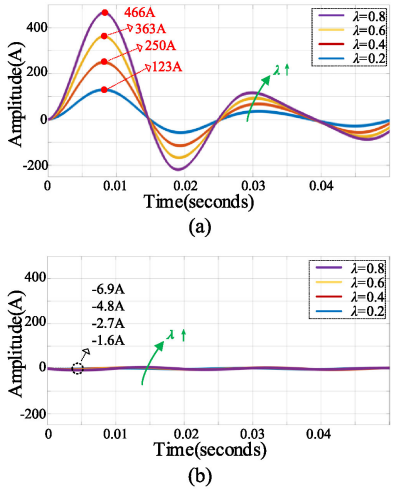

Fig. 14. Contrastive simulation results of transient inrush fault current in fault grid. (a) Voltage-controlled HSM in [17]–[20], $G = 5$. (b) Proposed CSM ($x = 5$, $y = 5.1$). (The solid blue line is $\lambda = 0.2$, the solid red line is $\lambda = 0.4$, the solid yellow line is $\lambda = 0.6$, the solid purple line is $\lambda = 0.8$.)

then $E = E_m$. So, the fundamental frequency impedance is not influenced by the improved VSG control, and the value of $Z_{\mathrm{sum},eqh}$ at fundamental frequency point should be considered.

According to the value of λ, the fundamental frequency impedance viewed from the PGF to VSG is finally expressed as

$$\begin{cases} Z_{\mathrm{sum},eqf} = k \cdot Z_{\mathrm{sum}}, & \lambda \geq \lambda_o \\ Z_{\mathrm{sum},eqf} = f_h \cdot Z_{\mathrm{sum}}, & \lambda < \lambda_o. \end{cases} \tag{28}$$

Based on (28), the curve of the fundamental frequency impedance $Z_{\mathrm{sum},eqf}$ with different λ is shown as Fig. 13. Obviously, if $\lambda\ \lambda_o$, the fundamental frequency impedance $Z_{\mathrm{sum},eqf}$ can be significantly increased by the improved VSG control, thus the steady-state fault current can be effectively restricted.

C. Limitation Effect of Transient Inrush Fault Current With the Proposed CSM

Since the impedance characteristic changes with frequency during short-circuit fault, it is not easy to obtain the nonlinear model for grid-connected DG. However, based on simulation, it is available to analyze the limitation effect of transient inrush fault current with the proposed CSM.

Fig. 14 shows the contrastive simulation results of transient inrush fault current in fault grid, where the voltage-controlled HSM in [17]–[20] is used in Fig. 14(a), $G = 5$; the proposed CSM ($x = 5$, $y = 5.1$) is used in Fig. 14(b); the different curve color represents different value of λ. As shown in Fig. 14(a), the amplitudes of transient inrush fault current reach several hundred amperes with the voltage-controlled HSM, and the larger λ is, the larger transient inrush fault current is. With the implement of the proposed CSM, the transient inrush fault current is effectively limited, as shown in Fig. 14(b). Therefore, the dynamic characteristic of transient inrush fault current and system stability can be effectively improved by the proposed CSM.

IV. Parameters Design of the Proposed CSM

In order to better analyze the coefficients ($-x$, y), the small-signal model of the VSG is established. Then, through the following three steps, the proper coefficients ($-x$, y) can be chosen according to both the system stability and the suppression effects of harmonic current and inrush fault current.

1) First, it is found that no matter how much x is taken, there must be $y \leq x + 1$ to ensure system stability.

Based on (1), the reactive power and active power output characteristic of VSG under small-signal disturbance can be obtained as

$$\Delta U_v = -\frac{0.707}{Ks + D_q}\Delta Q;\ \Delta\omega = s\Delta\theta = -\frac{1}{J\omega_N s + D_p\omega_N}\Delta P. \tag{29}$$

For simple analysis, ignoring the resistive components in the line, the active and reactive powers transmitted by the VSG is expressed as

$$P_e = \frac{U_v U_s \sin\theta}{Z_{\mathrm{sum},eqh}};\ Q_e = \frac{U_v U_s \cos\theta - U_s^2}{Z_{\mathrm{sum},eqh}}. \tag{30}$$

By linearizing (30), it can be obtained that

$$\begin{aligned} \Delta P_e &= \frac{\partial P}{\partial U_v}\cdot\Delta U_v + \frac{\partial P}{\partial\theta}\cdot\Delta\theta;\ \Delta Q_e \\ &= \frac{\partial Q}{\partial U_v}\cdot\Delta U_v + \frac{\partial Q}{\partial\theta}\cdot\Delta\theta \end{aligned} \tag{31}$$

where

$$\begin{cases} \frac{\partial P}{\partial U_v} = k_{p1} = \frac{U_s\sin\theta}{Z_{\mathrm{sum},eqh}}; & \frac{\partial P}{\partial\theta} = k_{p2} = \frac{U_v U_s\cos\theta}{Z_{\mathrm{sum},eqh}} \\ \frac{\partial Q}{\partial U_v} = k_{q1} = \frac{U_s\cos\theta}{Z_{\mathrm{sum},eqh}}; & \frac{\partial Q}{\partial\theta} = k_{q2} = -\frac{U_v U_s\sin\theta}{Z_{\mathrm{sum},eqh}}. \end{cases} \tag{32}$$

On the basis of (29), (31), and (32), the characteristic equation of the VSG small-signal closed-loop transfer function is

$$(k_{q1} + \sqrt{2}D_q + \sqrt{2}Ks)\cdot(J\omega_N s^2 + D_p\omega_N s + k_{p2}) = k_{p1}k_{q2} \tag{33}$$

where the equation order is very high and inconvenient to simplify, but its characteristic root locus can be drawled on MATLAB software.

Fig. 15 shows the characteristic root locus of closed-loop transfer function when $y = x+1$, where Fig. 15(a) and (b) uses ($x = 1$, $y = 2$) and ($x = 10$, $y = 11$), respectively. As shown in Fig. 15(a) and (b), there is always characteristic root (0, 0),

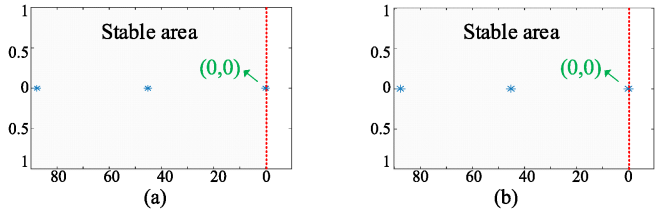

Fig. 15. Characteristic root locus of closed-loop transfer function when $y = x + 1$. (a) $x = 1$, $y = 2$. (b) $x = 10$, $y = 11$.

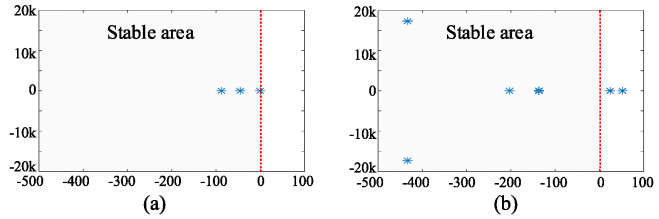

Fig. 16. Characteristic root locus of closed-loop transfer function when $x = 5$, $y \geq 6$. (a) $x = 5$, $y = 6$. (b) $x = 5$, $y = 7$.

and the system is critically stable. Moreover, when $y > 1 + x$, it is noted that the phase of $Z_{\mathrm{sum},eqh}$ turns reversal based on (21) and (22). That is, no matter how much x is taken, there must be $y \leq x + 1$ to ensure system stability.

2) Second, when $y = x + 1$, it is the worst situation for harmonic current suppression. In this case, the range of x can be obtained.

Based on (17), the bigger y is, the less the harmonic impedance viewed from the PCC to VSG is reduced. So, when $y = x+1$, the effect of harmonic suppression is the worst. Then, based on (18), i_{gh} can be derived as

$$i_{gh} \approx \frac{L_{v1}}{L_{v1} + L_s(1 + x)} i_{\mathrm{Loadh}}. \tag{34}$$

In this case, in order to obtain a better quality of grid current, it is expected that no more than 1/4 of the nonlinear load harmonic current flows into the grid. The range of x can be obtained as follows:

$$x \geq 3L_{v1}/L_s - 1. \tag{35}$$

According to the system parameters, the range of x can be obtained: $x \geq 5$, we take $x = 5$.

3) Third, it is found that when $x = 5$, y has maximum and minimum critical values to ensure system stability. To get better system stability, the median value is chosen.

Fig. 16 shows the characteristic root locus of closed-loop transfer function when $x = 5$, $y \geq 6$. As shown in Fig. 16(a), where $y = 6$, there is a characteristic root (0, 0), and the system is critically stable. As shown in Fig. 16(b), where y increases to $y = 7$, there are characteristic roots in right half-plane, and the system is unstable.

Fig. 17 shows the characteristic root locus of closed-loop transfer function when $x = 5$, $y \leq 4.1$. As shown in Fig. 17(a), where $y = 4.1$, there is a characteristic root (0, 0), and the system is critically stable. As shown in Fig. 17(b), where y decreases to

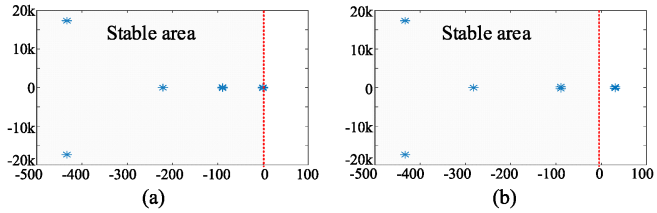

Fig. 17. Characteristic root locus of closed-loop transfer function when $x = 5$, $y \leq 4.1$. (a) $x = 5$, $y = 4.1$. (b) $x = 5$, $y = 0$.

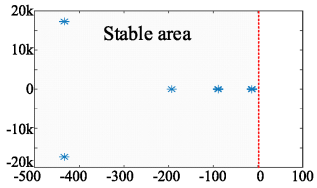

Fig. 18. Characteristic root locus of closed-loop transfer function when $x = 5$, $y = 5.1$.

TABLE I
SYSTEM PARAMETERS OF THE VSG

Parameters	Values	Parameters	Values
u_g/V	220	P_{set}/kW	10
f_g/Hz	50	Q_{set}/kW	0
f_s/Hz	20000	D_q	321
L_g/mH	1	D_p	5
L_s/mH	0.5	K	7.1
L_{v1}/mH	1	J/(kg·m^2)	0.057
Z_{line}/Ω	0.2	ω_N/(rad/s)	314.15926
C_f/uF	10	x	5
R_f/Ω	0.2	y	5.1

$y = 0$, there are characteristic roots in right half-plane, and the system is unstable.

A comprehensive analysis of Figs. 16 and 17 shows that when $4.1 = y_{\min} \leq y \leq y_{\max} = 6$, the system is stable. Meanwhile, when y is closer to the critical values $y_{\min}$ and $y_{\max}$, the system characteristic roots are closer to the imaginary axis, and the system stability is lower. So, in this paper, the median value ($y = 5.1$) is chosen to ensure better system stability.

Fig. 18 shows the characteristic root locus of the closed-loop transfer function when ($x = 5$, $y = 5.1$). As can be seen, the characteristic roots are in the left half-plane, and the system is stable. Therefore, when ($x = 5$, $y = 5.1$), the system can obtain optimal suppression effects of harmonic current and inrush fault current as well as the better system stability.

V. EXPERIMENTAL RESULTS

To verify the validity of the proposed CSM, a grid-connected DG system with VSG algorithm is built in the RTLAB platform. The system consists of thyristor rectifier load at PCC, and the grid short-circuit fault is realized by the earth impedance at the PGF. The system parameters are given in Table I.

Fig. 19 shows the contrastive experimental results of grid current after the nonlinear load introduced, where no HSM is

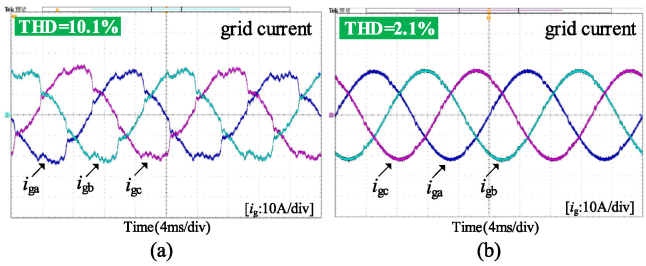

Fig. 19. Contrastive experimental results of grid current after nonlinear load introduced. (a) Without the HSM. (b) With the proposed CSM ($x = 5$, $y = 5.1$).

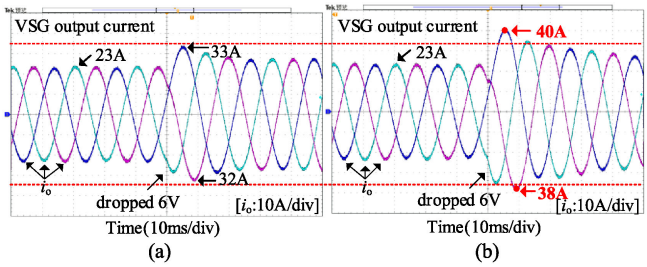

Fig. 20. Contrastive experimental results of VSG output current when grid voltage dropped by 6V. (a) Without the HSM. (b) With the voltage-controlled HSM in [17]–[20], $G = 5$.

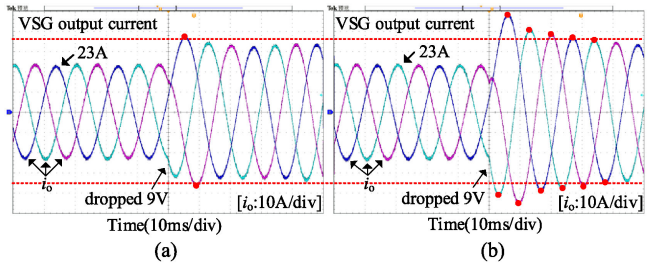

Fig. 21. Contrastive experimental results of VSG output current when grid voltage dropped by 9 V. (a) Without the HSM. (b) With the voltage-controlled HSM in [17]–[20], $G = 5$.

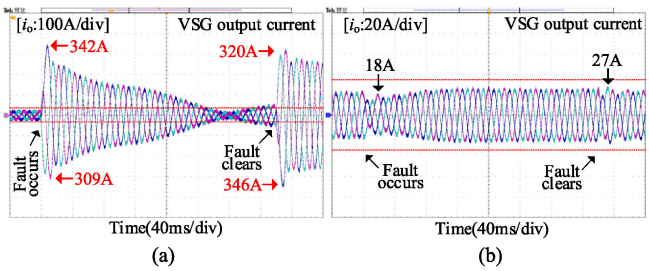

Fig. 22. Contrastive experimental results of VSG output current when grid voltage drops to 50% of the rated voltage. (a) Voltage-controlled HSM in [17]–[20], $G = 5$. (b) Proposed CSM ($x = 5$, $y = 5.1$).

used in Fig. 19(a); the proposed CSM ($x = 5$, $y = 5.1$) is used in Fig. 19(b). As shown in Fig. 19(a), the grid current is seriously distorted, and its THD reaches 10.1%. With the implement of the proposed CSM, as shown in Fig. 19(b), the harmonic current flowing into grid is effectively suppressed, and the THD of grid current is deduced to 2.1% since the nonlinear load harmonic current is mostly absorbed by the VSG.

Fig. 20 shows the contrastive experimental results of VSG output current when the grid voltage dropped by 6 V with the voltage-controlled HSM in [17]–[20], where no HSM is used in Fig. 20(a); the voltage-controlled HSM in [17]–[20] is used in Fig. 20(b), $G = 5$; the red dotted line is the safety limit value $\pm 1.5 \cdot \sqrt{2} I_{\mathrm{oN}} = \pm 34.5$ A. As shown in Fig. 20(a), the maximum amplitude of VSG output current increases from 23 to 33 A when the grid voltage dropped by 6 V, but the overcurrent protection is not activated since it does not exceed the safety limit of VSG output current. With the implement of this HSM, as shown in Fig. 20(b), the maximum amplitude of VSG output current increases to 40 A since the mid/high impedance viewed from the PGF to VSG is largely scaled down, so the overcurrent protection is activated. This means that the voltage-controlled HSM will aggravate the inrush fault current in the moment of grid symmetrical fault.

Fig. 21 shows the contrastive experimental results of VSG output current when the grid voltage dropped by 9 V with the voltage-controlled HSM in [17]–[20], where no HSM is used in Fig. 21(a); the voltage-controlled HSM in [17]–[20] is used in Fig. 21(b), $G = 5$; the red dotted lines is the safety limit value $\pm 1.5 \cdot \sqrt{2} I_{\mathrm{oN}} = \pm 34.5$ A. As shown in Fig. 21(a), there are two peak value points of VSG output current exceed the safety limit of VSG output current. With the implement of this HSM, as shown in Fig. 21(b), there are 11 peak value points of VSG output current exceed the safety limit of VSG output current since the mid/high impedance viewed from the PGF to the VSG is largely scaled down, so the overcurrent protection is more likely to be activated. This means that the voltage-controlled HSM can weaken the system's LVRT capability in the moment of grid symmetrical fault.

Fig. 22 shows the contrastive experimental results of VSG output current when the grid voltage drops to 50% of the rated voltage, where the voltage-controlled HSM in [17]–[20] is used in Fig. 22(a), $G = 5$; the proposed CSM ($x = 5$, $y = 5.1$) is used in Fig. 22(b). As shown in Fig. 22(a), the inrush fault current is severely aggravated by the voltage-controlled HSM, and the amplitude of transient inrush fault current reaches 346 A since the mid/high frequency impedance viewed from the PGF to VSG is small. As shown in Fig. 22(b), in the moment of fault occurring and clearing, the amplitudes of transient inrush fault current are reduced to 18 and 27 A, respectively, with the proposed CSM. These indicate that the steady-state and transient fault current can be effectively restricted by the proposed CSM without being affected by the voltage-controlled HSM.

Fig. 23 shows the contrastive experimental results of VSG output current when the grid voltage drops to 40% of the rated voltage, where the voltage-controlled HSM in [17]–[20] is used in Fig. 23(a), $G = 5$; the proposed CSM ($x = 5$, $y = 5.1$) is used in Fig. 23(b). As shown in Fig. 23(a), the inrush fault current is severely aggravated by the voltage-controlled HSM, and the amplitude of transient inrush fault current reaches 423 A since the mid/high frequency impedance viewed from the PGF to VSG is small. As shown in Fig. 23(b), in the moment of fault occurring

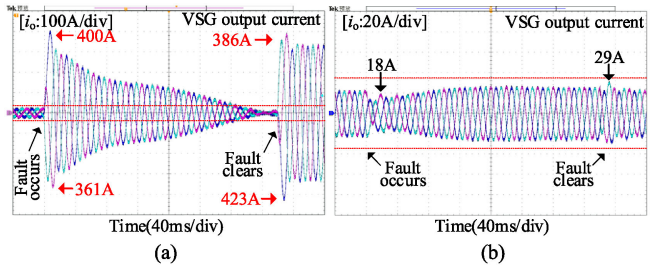

Fig. 23. Contrastive experimental results of VSG output current when grid voltage drops to 40% of the rated voltage. (a) Voltage-controlled HSM in [17]–[20], $G = 5$. (b) Proposed CSM ($x = 5$, $y = 5.1$).

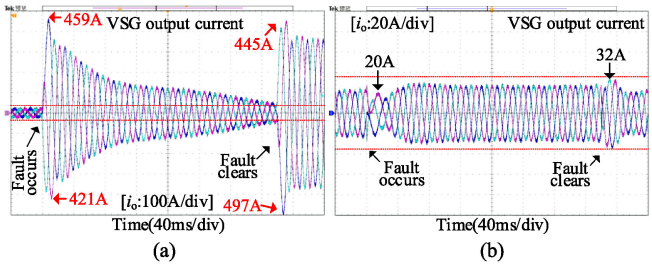

Fig. 24. Contrastive Experimental results of VSG output current when grid voltage drops to 30% of the rated voltage. (a) Voltage-controlled HSM in [17]–[20], $G = 5$. (b) Proposed CSM ($x = 5$, $y = 5.1$).

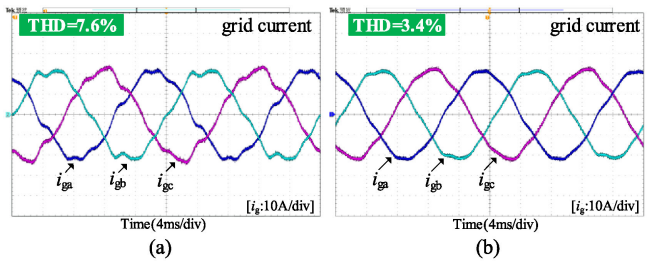

Fig. 25. Contrastive experimental results of grid current when grid voltage is distorted. (a) Without the HSM. (b) With the proposed CSM ($x = 5$, $y = 5.1$).

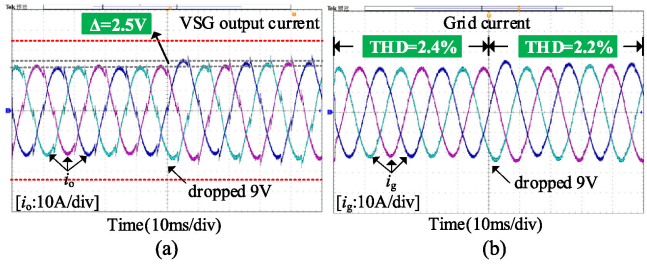

Fig. 26. Experimental results of VSG output current and grid current under the condition of nonlinear load and grid voltage dropped by 9V ($x = 5$, $y = 5.1$). (a) VSG output current. (b) Grid current.

and clearing, the amplitudes of transient inrush fault current are reduced to 18 and 29 A, respectively, with the proposed CSM. These indicate that the steady-state and transient fault current can be effectively restricted by the proposed CSM without being affected by the voltage-controlled HSM.

Fig. 24 shows the contrastive experimental results of VSG output current when the grid voltage drops to 30% of the rated voltage, where the voltage-controlled HSM in [17]–[20] is used in Fig. 24(a), $G = 5$; the proposed CSM ($x = 5$, $y = 5.1$) is used in Fig. 24(b). As shown in Fig. 24(a), the inrush fault current is severely aggravated by the voltage-controlled HSM, and the amplitude of transient inrush fault current reaches 497 A since the mid/high frequency impedance viewed from the PGF to VSG is small. As shown in Fig. 24(b), in the moment of fault occurring and clearing, the amplitudes of transient inrush fault current are reduced to 20 and 32 A, respectively, with the proposed CSM. These indicate that the steady-state and transient fault current can be effectively restricted by the proposed CSM without being affected by the voltage-controlled HSM.

Fig. 25 shows the contrastive experimental results of grid current when grid voltage is distorted, where no HSM is used in Fig. 25(a); the proposed CSM ($x = 5$, $y = 5.1$) is used in Fig. 25(b). As shown in Fig. 25(a), the grid current is severely distorted, and its THD reaches 7.6%. With the implement of the proposed CSM, as shown in Fig. 25(b), the grid harmonic current is apparently suppressed, and its THD is deduced to 3.4% since the mid/high frequency impedance as well as the harmonic impedance viewed from the grid to VSG are increased.

Fig. 26 shows the experimental results of VSG output current and grid current under the condition of nonlinear load and grid voltage dropped by 9 V, where Fig. 26(a) shows the waveform diagram of VSG output current; Fig. 26(b) shows the waveform diagram of grid current. As shown in Fig. 26(a), the maximum amplitude of VSG output current is limited to 24 A by the proposed CSM. As shown in Fig. 26(b), the THD of grid current before and after the grid voltage drop are 2.4% and 2.2%, respectively, since the harmonic impedance viewed from the PCC to the VSG is scaled down. Therefore, the proposed CSM can limit the VSG output fault current and maintain the power quality of grid current under the condition of both the nonlinear load introduced and the grid voltage dropped slightly.

VI. Conclusion

In this article, the adverse influence of the voltage-controlled HSM on the system's LVRT capability in the moment of grid symmetrical fault is found. To solve this issue, the harmonic current and inrush fault current CSM for the VSG is proposed, which mainly includes a passive branch, an active branch and an improved VSG control. The passive branch separated from the decentralized filter inductor is installed between the PCC and grid to introduce an additional voltage variable, which will not add the system power consumption. Through the proper feed-forwards of PCC voltage and additional voltage variable, the active branch cannot only reduce the harmonic impedance viewed from the PCC to VSG for absorbing the harmonic current introduced from the nonlinear load, but also increase the mid/high frequency impedance viewed from the PGF to VSG for limiting the transient inrush fault current. The improved VSG control is used to limit the steady-state fundamental frequency fault current. Therefore, the fault current restraint will not be

affected by the voltage-controlled HSM in the moment of grid symmetrical fault. Finally, the experiment results validate the proposed CSM in the RTLAB platform.

APPENDIX

Based on (1), the reactive power control equation of VSG is expressed as

$$D_q(\sqrt{2}U_{\text{nom}} - \sqrt{2}U_o) + Q_{\text{set}} - Q_e = K\frac{d\sqrt{2}E_m}{dt}. \quad (36)$$

During the fault, ΔQ represents the change of VSG instantaneous reactive power; ΔE_m represents the change of VSG inner electric potential rms; ΔU_o represents the change of VSG output voltage rms; ΔI_o represents the change of VSG output current rms; and Z_v represents the VSG output impedance. Then, there is $\Delta E_m = \Delta U_o + \Delta I_o \cdot Z_v$. It can be derived as

$$D_q(-\Delta E_m - \Delta I_o \cdot Z_v) + \frac{\Delta Q}{\sqrt{2}} = K\frac{d\Delta E_m}{dt}. \quad (37)$$

Solving this equation, it can be gotten that

$$\begin{aligned}\Delta E_m &= \frac{\Delta Q/\sqrt{2 - D_q\Delta I_o \cdot Z_v}}{D_q}\left(1 - e^{-\frac{D_q}{K}t}\right)\\ &\approx \frac{\Delta Q}{\sqrt{2}D_q} - \Delta I_o \cdot Z_v \end{aligned} \quad (38)$$

where, $e^{-D_q t/K} \to 0$ can be ignored.

So, the change of VSG output voltage rms is expressed as

$$\Delta U_o = \Delta E_m - \Delta I_o \cdot Z_v \approx \frac{\Delta Q}{\sqrt{2}D_q}. \quad (39)$$

Based on (1), the active power control equation of VSG is obtained as

$$\begin{cases}\frac{d\theta}{dt} = \omega_o - \omega_N \\ J\omega_N\frac{d\omega_o}{dt} = P_{set} - P_e - D_p\omega_N(\omega_o - \omega_N).\end{cases} \quad (40)$$

During the fault, ΔP represents the change of VSG instantaneous active power; $\Delta\omega$ represents the change of VSG output angular frequency; and $\Delta\theta$ represents the change of VSG phase angle. It can be derived as

$$\frac{d\Delta\omega}{dt} + \frac{D_p}{J}\Delta\omega = \frac{\Delta P}{J\omega_N}. \quad (41)$$

Solving this equation, it can be gotten that

$$\Delta\omega = \frac{\Delta P}{D_{\text{p}}\omega_{\text{N}}}(1 - e^{-\frac{D_{\text{p}}}{J}t}) \approx \frac{\Delta P}{D_{\text{p}}\omega_{\text{N}}} \quad (42)$$

where $e^{-D_p t/J} \to 0$ can be ignored.

So, the change of VSG phase angle is expressed as

$$\Delta\theta = \int \Delta\omega dt \approx \frac{\Delta P}{D_p\omega_N}t. \quad (43)$$

For the VSG without voltage closed-loop control, it can be considered that the VSG terminal voltage u_v is approximately equal to the voltage reference of VSG (u^*_{v}) for simple analysis. Based on (39) and (43), when considering the effects of inertia and damping characteristics of VSG, the changed terminal voltage is expressed as

$$u_v \approx u_v^* = \sqrt{2}(U_v + \Delta U_o)\sin(\omega_N t + \theta + \Delta\theta). \quad (44)$$

The PGF voltage after the fault is expressed as follows:

$$u_{sf} = \sqrt{2}U_{sf}\sin(\omega_N t) = \sqrt{2}(1-\lambda)U_s\sin(\omega_N t) \quad (45)$$

where u_{sf} and u_s represent, respectively, the PGF voltages after and before the fault; U_{sf} and U_s represent the rms values of u_{sf} and u_s, respectively; and λ represents the voltage drop depth at the PGF.

Based on (44) and (45), if the VSG terminal voltage change is considered, the voltage drop from VSG to PGF is expressed as

$$\begin{aligned}\Delta u_f = \sqrt{2}(1-\lambda)U_s\sin(\omega_N t) - \sqrt{2}(U_v + \Delta U_o)\\ \times\sin(\omega_N t + \theta + \Delta\theta).\end{aligned} \quad (46)$$

Meanwhile, if the VSG terminal voltage change is not considered, the voltage drop from the VSG to PGF is expressed as

$$\Delta u = \sqrt{2}(1-\lambda)U_s\sin(\omega_N t) - \sqrt{2}U_v\sin(\omega_N t + \theta). \quad (47)$$

When λ = (0.4, 0.6, 0.8), the waveform of Δu_f and Δu are shown as Fig. 27(a)–(c), the deviation ratio ($\Delta\% = (\Delta u_f - \Delta u)/\Delta u$) are 1.80%, 2.73%, 5.53%, respectively. For convenience, it can be approximated as $\Delta u \approx \Delta u_f$. Therefore, according to Fig. 27, it is found that the voltage drop from the VSG to PGF mainly depends on the voltage drop at the PGF.

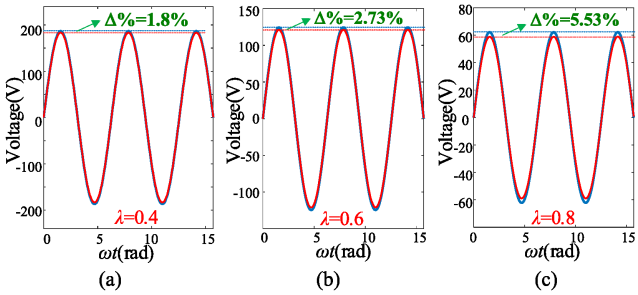

Fig. 27. Waveform of Δu_f and Δu under different voltage drop depth. (a) λ = 0.4. (b) λ = 0.6. (c) λ = 0.8. (The solid blue line is Δu_f, and the solid red line is Δu.)

REFERENCES

[1] Q. Zhong, P. L. Nguyen, Z. Ma, and W. Sheng, "Self-synchronized synchronverters: Inverters without a dedicated synchronization unit, " *IEEE Trans. Power Electron.*, vol. 29, no. 1, pp. 617–630, May 2014.

[2] L. Harnefors, "Modeling of three-phase dynamic systems using complex transfer functions and transfer matrices," *IEEE Trans. Ind. Electron.*, vol. 54, no. 4, pp. 2239–2248, Aug. 2007.

[3] H. Wu *et al.*, "Small-signal modeling and parameters design for virtual synchronous generators," *IEEE Trans. Ind. Electron.*, vol. 63, no. 7, pp. 4292–4303, Mar. 2016.

[4] B. Wen, D. Boroyevich, R. Burgos, P. Mattavelli, and Z. Shen, "Analysis of D-Q small-signal impedance of grid-tied inverters," *IEEE Trans. Power Electron.*, vol. 31, no. 1, pp. 675–687, Jan. 2015.

[5] F. Blaabjerg, R. Teodorescu, M. Liserre, and A. V. Timnus, "Overview of control and grid synchronization for distributed power generation systems," *IEEE Trans. Ind. Electron.*, vol. 53, no. 5, pp. 1398–1409, Oct. 2006.

[6] F. Wang, J. L. Duarte, M. A. Hendrix, and P. F. Ribeiro, "Modelling and analysis of grid harmonic distortion impact of aggregated DG inverters," *IEEE Trans. Power Electron.*, vol. 26, no. 3, pp. 786–797, Mar. 2011.
[7] B. Renders, K. Gusseme, W. Ryckaert, K. Stockman, L. Vandevelde, and M. H. J. Bollen., "Distributed generation for mitigating voltage dips in low-voltage distribution grids," *IEEE Trans. Power Del.*, vol. 23, no. 3, pp. 1581–1588, Jul. 2008.
[8] H. Zhou, Y. Li, N. R. Zargari, Z. Cheng, R. Ni, and Y. Zhang, "Selective harmonic compensation (SHC) PWM for grid-interfacing high-power converters," *IEEE Trans. Power Electron.*, vol. 29, no. 3, pp. 1118–1127, Mar. 2014.
[9] Y. Zhang, Y. W. Li, N. Zargari, and Z. Cheng, "Improved selective harmonics elimination scheme with online harmonic compensation for high-power PWM converters," *IEEE Trans. Power Electron.*, vol. 30, no. 7, pp. 3508–3517, Aug. 2014.
[10] T. Takeshita and N. Matsui, "Current waveform control of PWM converter system for harmonic suppression on distribution system," *IEEE Trans. Ind. Electron.*, vol. 50, no. 6, pp. 1134–1139, Dec. 2003
[11] Z. Ali, N. Christofides, L. Hadjidemetriou, and E. Kyriakides, "Diversifying the role of distributed generation grid side converters for improving the power quality of distribution networks using advanced control techniques," *IEEE Trans. Ind. Appl.*, vol. 55, no. 4, pp. 4110–4123, Aug. 2019.
[12] W. Wu *et al.*, "Sequence impedance modeling and stability comparative analysis of voltage-controlled VSGs and current-controlled VSGs," *IEEE Trans. Ind. Electron.*, vol. 66, no. 8, pp. 6460–6472, Aug. 2019.
[13] A. D. Paquette and D. M. Divan, "Virtual impedance current limiting for inverters in microgrids with synchronous generators," *IEEE Trans. Ind. Appl.*, vol. 51, no. 2, pp. 1630–1638, Aug. 2014.
[14] X. Wang, F. Blaabjerg, and Z. Chen, "Synthesis of variable harmonic impedance in inverter-interfaced distributed generation unit for harmonic damping throughout a distribution network," *IEEE Trans. Ind. Appl.*, vol. 48, no. 4, pp. 1407–1417, Jul./Aug. 2012.
[15] P. Sreekumar and V. Khadkikar, "A new virtual harmonic impedance scheme for harmonic power sharing in an islanded microgrid," *IEEE Trans. Power Del.*, vol. 31, no. 3, pp. 936–945, Jun. 2016.
[16] X. Zhang, Q. Zhong, and W. Ming, "Stabilization of a cascaded dc converter system via adding a virtual adaptive parallel impedance to the input of the load converter," *IEEE Trans. Power Electron.*, vol. 31, no. 3, pp. 1826–1832, Mar. 2016.
[17] J. He, Y. W. Li, and M. S. Munir, "A flexible harmonic control approach through voltage-controlled DG-grid interfacing converters," *IEEE Trans. Ind. Electron.*, vol. 59, no. 1, pp. 444–455, Jan. 2012.
[18] J. He, Y. W. Li, J. M. Guerrero, F. Blaabjerg, and J. C. Vasquez, "An islanding microgrid power sharing approach using enhanced virtual impedance control scheme," *IEEE Trans. Power Electron.*, vol. 28, no. 11, pp. 5272–5282, Nov. 2013.
[19] X. Zhao, L. Meng, C. Xie, J. M. Guerrero, and X. Wu, "A unified voltage harmonic control strategy for coordinated compensation with VCM and CCM converters," *IEEE Trans. Power Electron.*, vol. 33, no. 8, pp. 7132–7147, Aug. 2018.
[20] T. Wang, H. Nian, Z. Q. Zhu, L. Ding, and B. Zhou, "Flexible compensation strategy for voltage source converter under unbalanced and harmonic condition based on a hybrid virtual impedance method," *IEEE Trans. Power Electron.*, vol. 33, no. 9, pp. 7656–7673, Sep. 2018.
[21] A. Camacho, M. Castilla, J. Miret, A. Borrell, and L. García de Vicuña, "Active and reactive power strategies with peak current limitation for distributed generation inverters during unbalanced grid faults," *IEEE Trans. Ind. Electron.*, vol. 62, no. 3, pp. 1515–1525, Aug. 2015.
[22] K. Shi *et al.*, "Low-voltage ride through control strategy of virtual synchronous generator based on the analysis of excitation state," *IET Gener. Transmiss. Distrib.*, vol. 12, no. 9, pp. 2165–2172, Mar. 2018.
[23] K. Oureilidis and C. Demoulias, "A fault clearing method in converter-dominated microgrids with conventional protection means," *IEEE Trans. Power Electron.*, vol. 31, no. 6, pp. 4628–4640, Sep. 2015.
[24] K. Shi, W. Song, P. Xu, R. Liu, Z. Fang, and Y. Ji, "Low-voltage ride through control strategy for a virtual synchronous generator based on smooth switching," *IEEE Access*, vol. 6, pp. 2703–2711, Dec. 2018.
[25] M. Liu *et al.*, "An enhanced virtual synchronous generator strategy for suppressing grid voltage sag," in *Proc. 2016 IEEE Power Energy Soc. Gen. Meeting*, Kaohsiung, Taiwan, Jun. 2017, pp. 2064–2069.
[26] M. Jafari, S. B. Naderi, M. T. Hagh , M. Abapour, and S. H. Hosseini, "Voltage sag compensation of point of common coupling (PCC) using fault current limiter," *IEEE Trans. Power Del.*, vol. 26, no. 4, pp. 2638–2646, Aug. 2011.
[27] Y. W. Li, D. M. Vilathgamuwa, P. C. Loh, and F. Blaabjerg, "A dual functional medium voltage level DVR to limit downstream fault currents," *IEEE Trans. Power Electron.*, vol. 22, no. 4, pp. 1330–1340, Jul. 2007.
[28] Z. Shuai, W. Huang, C. Shen, J. Ge, and Z. John Shen., "Characteristics and restraining method of fast transient inrush fault currents in synchronverters," *IEEE Trans. Ind. Electron.*, vol. 64, no. 9, pp. 7487–7497, Jan. 2017.
[29] J. He and Y. W. Li, "Analysis, design, and implementation of virtual impedance for power electronics interfaced distributed generation," *IEEE Trans. Ind. Appl.*, vol. 47, no. 6, pp. 2525–2538, Nov./Dec. 2011.
[30] D. M. Vilathgamuwa, P. C. Loh, and Y. W. Li, "Protection of microgrids during utility voltage sags," *IEEE Trans. Ind. Electron.*, vol. 53, no. 5, pp. 1427–1436, Oct. 2006.
[31] D. Zmood, D. Holmes, and G. Bode, "Frequency-domain analysis of three-phase linear current regulators," *IEEE Trans. Ind. Electron.*, vol. 37, no. 2, pp. 601–610, Mar./Apr. 2001.

Leming Zhou (Member, IEEE) was born in Hunan, China, in 1989. He received the B.S. and Ph.D. degrees in electrical engineering from Hunan University, Changsha, China, in 2011 and 2016, respectively.

He is currently a Postdoctoral Research in electrical engineering with Hunan University. His research interests include power electronics, electric power green transformation, distributed generation, and marine special power supply.

Siyi Liu (Student Member, IEEE) was born in Hubei, China, in 1997. She received the B.S. degree from the College of Information and Control Engineering, China University of Petroleum, Qingdao, China, in 2014. She is currently working toward the M.S. degree in electrical engineering with Hunan University, Changsha, China.

Her research interests include power electronics, grid-connected inverter, and power quality.

Yandong Chen (Senior Member, IEEE) was born in Hunan, China, in 1979. He received the B.S. and M.S. degrees in instrument science and technology from Hunan University, Changsha, China, in 2003 and 2006, respectively, and the Ph.D. degree in electrical engineering from Hunan University, Changsha, China, in 2014.

He is currently an Associate Professor with the College of Electrical and Information Engineering, Hunan University. His research interests include power electronics for microgrid, distributed generation, power quality, and energy storage.

Dr. Chen is a recipient of the 2014 National Technological Invention Awards of China, and the 2014 WIPO-SIPO Award for Chinese Outstanding Patented Invention. He is a member of IEEE Power Electronics Society.

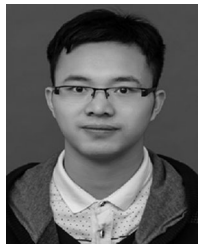

Weilang Yi (Student Member, IEEE) was born in Hunan, China, in 1991. He received the B.S. and M.S. degrees in 2015 and 2018, respectively, from the College of Electrical and Information Engineering, Hunan University, Changsha, China, where he is currently working toward the Ph.D. degree in electrical engineering.

His current research interests include microgrid, power quality, and special power supply.

Shuke Wang (Student Member, IEEE) was born in Henan, China, in 1996. He received the B.S. degree in 2019 from the College of Electrical and Information Engineering, Hunan University, Changsha, China, where he is currently working toward the Ph.D. degree in electrical engineering.

His current research interests include power quality control, distributed generation, and power electronics for microgrid.

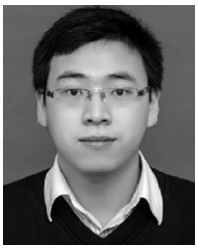

Xiaoping Zhou (Member, IEEE) was born in Jiangxi, China, 1990. He received the B.S. degree in electrical engineering in 2013 from Hunan University, Changsha, China, where he is currently working toward the Ph.D. degree in electrical engineering.

His research interests include power electronics, distributed generation, microgrid, energy storage, and management.

Wenhua Wu (Member, IEEE) was born in Hunan, China, 1991. He received the B.S. degree in 2014 from the College of Electrical and Information Engineering, Hunan University, Changsha, where he is currently working toward the Ph.D. degree in electrical engineering.

His research interests include renewable energy generation systems, microgrid, power quality, and VSC-HVdc systems.

Jie Zhou (Student Member, IEEE) was born in Hunan, China, 1997. He received the B.S. degree in 2019 from the College of Electrical and Information Engineering, Hunan University, Changsha, China,where he is currently working toward the M.S. degree in electrical engineering.

His research interests include power electronics, microgrid, energy management.

Chan Xiao was born in Hunan, China, 1994. She received the B.S. degree from the College of Electrical and Automation, Huazhong University of Science and Technology Wuchang Branch, Wuhan, China, in 2015. She is currently working toward the M.S. degree in electrical engineering with Hunan University, Changsha, China.

Her research interests include power electronics, electric power green transformation, and distributed generation.

Aoyang Liu was born in Hunan, China, in 1991. He received the M.S. degree from the College of Electrical and Information Engineering, Hunan University, Changsha, China, in 2019.

His current research interests include microprocessor based protective relay.